New (α β γ)-incommensurate magnetic phase discovered in the $MnCr_2O_4$ spinel at low temperatures.

M. Pardo-Sainz,[1,2] A. Toshima,[3] G. André,[4] J. Basbus,[5] G. J. Cuello,[6] V. Laliena,[7] T. Honda,[8] T. Otomo,[8] K. Inoue,[9] Y. Hosokoshi,[2] Y. Kousaka,[10,*] and J. Campo[1,†]

[1] *Aragón Nanoscience and Materials Institute (CSIC – University of Zaragoza) and Condensed Matter Physics Department, C/Pedro Cerbuna 12, 50009 Zaragoza, Spain*
[2] *Graduate School of Science, Osaka Metropolitan University, Osaka 599-8531, Japan*
[3] *Research Institute for Interdisciplinary Science, Okayama University, Okayama, Japan*
[4] *Laboratoire Léon Brillouin, Saclay, France*
[5] *Centro Atómico Bariloche, S. C. de Bariloche, Rio Negro, Argentine*
[6] *Institut Laue-Langevin, Grenoble, France*
[7] *Applied Mathematics Department of the University of Zaragoza, Zaragoza, Spain*
[8] *Institute of Materials Structure Science, Tsukuba, Japan*
[9] *Graduate School of Science, Chirality Research Center and International Institute for Sustainability with Knotted Chiral Meta Matter, Hiroshima University, Japan*
[10] *Department of Physics and Electronics, Osaka Metropolitan University, Osaka 599-8531, Japan*

(Dated: March 15, 2023)

The nuclear and magnetic structure of the spinel $MnCr_2O_4$ is reinvestigated by magnetization, specific heat and neutron diffraction experiments at different temperatures. Four samples of this spinel synthesized under different atmospheres are analysed. Through these experiments a new magnetic phase, with propagation vector $\vec{k}_{\rm I2} = (0.6597(1)\, 0.5999(1)\, 0.1996(2))$, not previously reported, is identified below 18 K when the sample is synthesized under a reductive atmosphere. A possible explanation for the different magnetic ground states observed is given based on the competition among the main exchange interactions present in the system. Using the magnetic superspace group formalism, the symmetry of the nuclear and magnetic structures is determined. The presence of transverse conical magnetic structures in the lower-temperature phases allows for multiferroicity in this compound, and the electric polarization direction is determined for each magnetic phase.

I. INTRODUCTION

Nowadays, chromium-based normal spinel oxides ACr_2O_4, where A is a divalent cation, are among the most studied materials in the condensed matter community due to the interplay between their magnetic, electric and structural properties as well as to their potential application to different key industry sectors, such as magnetic refrigerators, super-capacitors, solid oxide fuel cells, lithium-oxygen battery electrodes, catalytic materials and magnetic devices [1–8]. In these compounds, several physical behaviours have been observed, which include magnetostriction, colossal magnetoresistance, multiferroicity, spin frustration and others [5, 9–24].

These chromium spinel oxides crystallize with the normal cubic spinel structure, space group (SG) $Fd\bar{3}m$, at high temperatures. In this structure, the tetrahedral A-sites are occupied by A^{2+} cations forming a diamond sublattice, while the octahedral B-sites are occupied by Cr^{3+} (S=3/2) cations forming a pyrochlore sublattice (see Fig. 1). The local crystal field produced by the oxygen anions O^{2-} splits the $3d$ orbitals of the Cr^{3+} cation into a low-lying t_{2g} triplet and a higher-energy e_g doublet, while the orbitals of the A^{2+} cations are split into a lower e_g doublet and a higher t_{2g} triplet [19, 25, 26].

In these systems, the main magnetic interaction is the strong $J_{\rm CrCr}$ antiferromagnetic direct exchange between the nearest neighbours cations [19, 25, 27, 28]. This interaction leads to a highly frustrated ground state on the pyrochlore sublattice. This frustration can only be released by the so-called spin-Jahn-Teller effect for compounds with non-magnetic A cations, where lattice distortions induce differences between the exchange coefficients originally uniform for each Cr^{3+}-Cr^{3+} pair. In contrast, if A cations are magnetic, the coupling of Cr^{3+} spins to the A cations spins on the bipartite diamond lattice removes the magnetic frustration, and the system apparently maintains the nearly cubic structure even in its low temperature magnetic state [12, 15, 19, 22, 23, 26, 29–32]. In this case, the Curie-Weiss temperatures ($\Theta_{\rm CW}$) in ACr_2O_4 were found to be significantly higher than the long-range magnetic ordering (LRO) temperature ($T_{\rm N}$) for the non-Jahn-Teller magnetic cations (A=Mn, Co) [12, 19]. This ratio $|\Theta_{\rm CW}|/T_{\rm N}$ measures the degree of magnetic frustration. An schema of the nuclear structure of $MnCr_2O_4$ is depicted in Fig.1.

For the cubic spinel systems (AB_2O_4), a theory of the ground state spin configuration was presented by Lyons, Kaplan, Dwight, and Menyuk (LKDM) almost 60 years ago [33] describing complex magnetic orders. In this theory, the degree of magnetic frustration is represented by the parameter $u = 4J_{\rm BB}S_{\rm B}/3J_{\rm AB}S_{\rm A}$, where $J_{\rm BB}$, $J_{\rm AB}$ are the nearest-neighbour exchange interactions between spins $S_{\rm B}$ and $S_{\rm A}$ on the A and B sites. The possible val-

* koyu@omu.ac.jp
† javier.campo@csic.es

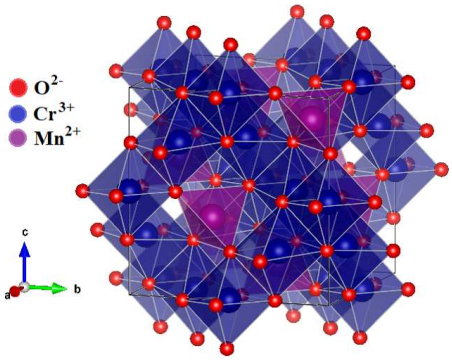

FIG. 1. Nuclear structure of $MnCr_2O_4$ showing the octahedral (CrO_6), in blue, and tetrahedral (MnO_4), in purple, positions.

ues of u describe different magnetic structures, ranging from a Néel collinear configuration for $u \leq u_0 = 8/9$, to a LRO spiral structure, which is locally stable for $u_0 < u < u"\approx 1.298$, but unstable if $u > u"$. In particular, for $MnCr_2O_4$, where the A^{2+} ions are Mn^{2+} (S=5/2), the values reported for u are 1.6 [29] and 1.5 [12]. However, the importance of the J_{AA} exchange interaction in determining the spiral order has also been highlighted [19, 25, 27, 34, 35], since the LKDM theory does not take it into account.

Neutron diffraction studies reported that $MnCr_2O_4$ shows a ferrimagnetic LRO (FIM), with an easy axis parallel to the $\langle 1\bar{1}0\rangle$ direction, below $T_N \sim 41$ K. When the temperature decreases below $T_I \sim 18$ K, this ferrimagnetic phase coexists with a spiral short-range order (SRO) given by a propagation vector parallel to the $\langle 110\rangle$ direction [12, 29, 34, 36]. Electron paramagnetic resonance (ESR) experiments were also compatible with the neutron scattering experiments [19, 37]. However dielectric measurements, in addition to the anomalies found at T_N and T_I in other reports, showed signatures of a lock-in temperature at $T_F \sim 14$ [38].

Recently, Lin *et al.* [32] with magneto-electric, heat capacity and Raman spectroscopy studies on $MnCr_2O_4$ claimed for the existence of a first order magnetic phase transition from an incommensurate to commensurate state below $T_F \sim 17$ K anticipating that the oxygen content could be a key factor determining the magnetic ground state. These "unconventional" proposed magnetic orders at low temperatures also induce ferroelectricity, as has been reported in [23, 32].

However, there is not a definitive answer yet on the range of the measured incommensurate spiral phase appearing below T_N neither the existence of a new commensurate phase at the lowest temperatures as proposed [32]. Moreover, no systematic study has been reported on the role of the synthesis conditions on the magneto-structural properties in $MnCr_2O_4$.

Therefore, in this paper we reinvestigate the nuclear and magnetic structures of the $MnCr_2O_4$ as function of the temperature (T) in powder samples synthesized under different conditions by using magnetization, specific heat and neutron powder diffraction (NPD) experiments. Our results confirms the existence of three LRO magnetic phases; a FIM with propagation vector $\vec{k}_N = (0\,0\,0)$, an incommensurate spiral phase with $\vec{k}_{I1} = (\delta\,\delta\,0)$, and a new one, never reported, with $\vec{k}_{I2} = (\alpha\,\beta\,\gamma)$. The transition temperatures of these phases depend on the oxidizing or reductive atmosphere in which the samples were synthesized.

The magnetic superspace group (MSSG) formalism [39–41] used in this work allows for the complete determination of the global symmetry of the system (both of the magnetic and nuclear contributions) expressed with crystallographic rules. An explanation of these transitions based on experimental and theoretical results is also discussed.

II. SAMPLE PREPARATION AND EXPERIMENTAL DETAILS

Four different batches of micro-crystalline powder of $MnCr_2O_4$ were prepared under different synthetic conditions. All samples were obtained by the solid phase reaction method, in which powder of MnO and Cr_2O_3 with molar ratio 1:1 were mixed and heated up to 1200 °C for a time, t, under a reductive atmosphere, with Ar and H_2 with ratio 20:1, (samples S1R and S2R) or oxidizing, in atmospheric air conditions, (samples S1A and S2A). The annealing time t was 48 hours for samples S1R and S1A and 24 hours for samples S2R and S2A.

Preliminary structural characterization at room temperature (RT) indicated that reductive samples (S1R and S2R) included only $MnCr_2O_4$, while for the oxidizing samples (S1A and S2A) also a minority impurity phase of Cr_2O_3 appeared.

An additional single crystal of $MnCr_2O_4$, with a mass of 2.8 mg and labelled SC1R, employed in the heat capacity and some magnetization measurements, was prepared by a laser-diode-heated floating zone furnace (equipped with five 200 W lasers, Crystal Systems Corporation). To minimize evaporation of MnO in the crystal growth, the crystal growth was performed under 0.6 MPa of Ar atmosphere, and travelling speeds of feed and seed rods were set to be 20–22 mm/h. To compensate for the evaporation, the polycrystalline feed rod composed of MnO and Cr_2O_3 in the molar ratio of 1.25:1.

The specific heat of SC1R at zero field and the magnetic properties of all the samples, were measured, respectively, in a physical properties measurement system (PPMS-9T) and a magnetic properties measurement system (MPMS-XL5), both manufactured by Quantum Design.

NPD experiments in S1R were performed at different temperatures (1.6 K $\leq T \leq$ 300 K), on the two-axis spectrometer G.4.1, installed at the cold neutron guide

G4 of the Laboratoire Léon Brillouin in Saclay, France. The wavelength of the incident neutrons was fixed at $\lambda = 2.419$ Å. A pyrolytic graphite filter efficiently eliminated higher-order contamination. The diffractograms were collected in an angular range from $5.0° \leq 2\theta \leq 85°$.

For S1A, S2R and S2A samples the NPD experiments were performed at different temperatures (5 K $\leq T \leq$ 300 K) on the High Intensity Total Diffractometer NOVA, installed at the thermal guide BL21 of the Materials and Life Facility (MLF) in Tokai, Japan. We focus our analysis on the data set corresponding to the bank at $2\theta = 90°$, at which it is possible to observe the magnetic satellite peaks with the highest resolution possible. Additional measurements in S1R and S1A were also performed at S-HRPD (Super High Resolution Powder Diffractometer), installed at the thermal guide BL08 of MLF.

III. RESULTS

A. Magnetization and heat capacity experiments

Magnetization versus temperature measurements have been done for all the four samples under the zero field cooling (ZFC) and field cooling (FC) modes with applied magnetic field $H = 200$ Oe, as it is depicted in Fig. 2. In all cases a sudden increase in the magnetization as the temperature decreases is observed at around $T_N = 41$ K, indicating a transition from the paramagnetic (PM) to a FIM state. The transition temperature T_N for each sample is shown in Fig. 2 with a purple vertical line.

In S1R and S2R two anomalies at $T_{I1} \approx 20$ K and $T_{I2} \approx 18$ K are observed (see the insert in Fig. 2 (a) and (c)). The magnetization curves for S1A and S2A show also two anomalies at lower temperatures at $T_{I1} \approx 19$ K and $T_L \approx 16$ K, this one more visible in the ZFC curves. T_{I1}, T_{I2} and T_L are showed in the insert of Fig. 2 with vertical blue, pink and grey lines.

The inverse susceptibility at high temperatures was fitted to a characteristic expression for ferrimagnetic ordering [19, 42, 43], given by:

$$\frac{1}{\chi} = \frac{T - \Theta_{CW}}{C} - \frac{\eta}{T - \theta_h}, \qquad (1)$$

where C is the Curie constant, Θ_{CW} is the Curie-Weiss temperature. The first term is the high-T asymptote that has a Curie-Weiss form, and the second term is the hyperbolic low-T asymptote in which η and θ_h are functions of the molecular field coefficients defining the interactions between the A and B sub-lattices. The fitted $\chi^{-1}(T)$ for S2R by Eq.(1) gives the values $C = 7.79(3)$ emu K/mol, $\Theta_{CW} = -427(3)$ K, $\eta = 1707(16)$ mol K/emu, and $\theta_h = 26.8(2)$ K. The effective magnetic moment is determined to be $\mu_{eff} \sim 7.89(3)\,\mu_B$ ($\mu_{eff} = \mu_B\sqrt{3k_BC/N_A}$), which is close to the theoretical value ($\mu_{theo} = 8.04\,\mu_B$) expected for high-spin Cr^{3+} (S = 3/2) and Mn^{2+} (S = 5/2). The ratio of $|\Theta_{CW}|/T_N \sim 10$ indicates a significant magnetic frustration due to competing J_{CrCr}, J_{MnMn}, and J_{MnCr} exchange interactions at low temperatures.

Following the same analysis as was carried out by Winkler *et al.* [19], we can use a Weiss mean-field (MF) model and relate the fitted parameters from Eq.(1) with the AFM exchange constants between sublattices, thus obtaining: J_{CrCr} = -38.0(5) K, J_{MnMn} = -8.4(2) K and J_{MnCr} = -13.9(2) K. From these values we can calculate

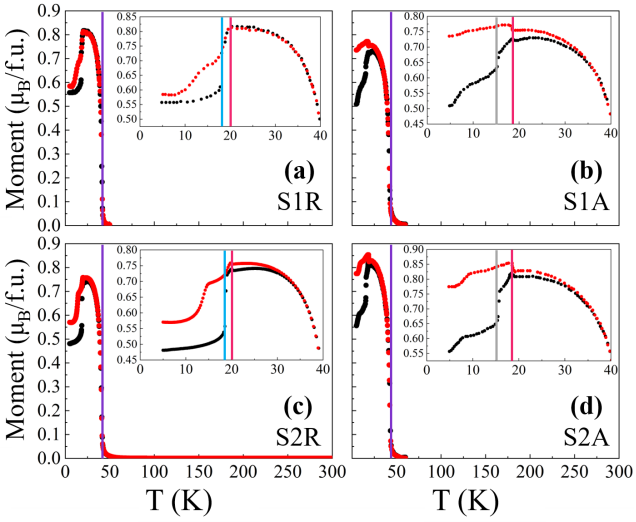

FIG. 2. Temperature dependence of the magnetization with an applied magnetic field $H = 200$ Oe measured after zero field cooling (ZFC) (black dots) and field cooling (FC) (red dots) procedures for samples S1R (a), S1A (b), S2R (c) and S2A (d). T_N is showed with a purple line, while T_{I1}, T_{I2} and T_L are showed with blue, pink and grey lines in the inserts.

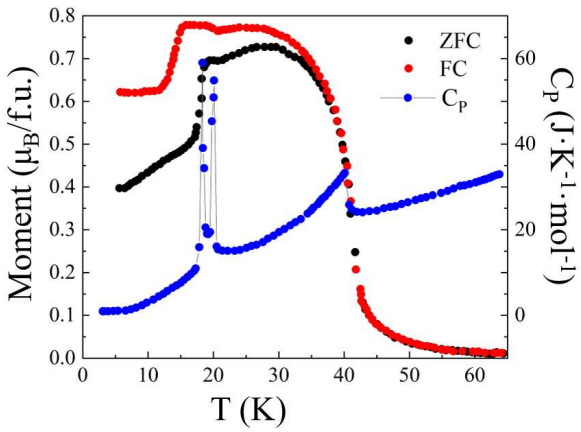

FIG. 3. Temperature dependence of heat capacity C_P (blue dots) at zero field and ZFC (black dots) and FC (red dots) magnetization curves at $H = 200$ Oe for SC1R sample. The heat capacity curve shows clearly three transitions temperatures $T_N = 40$ K, $T_{I1} = 20$ K and $T_{I2} = 18$ K.

the ratio $R \approx J_{\mathrm{CrCr}}/J_{\mathrm{MnCr}} \sim 2.74(4)$, which is slightly different to the reported values $R \approx 3$ [28] and 3.02 [19].

The temperature-dependent magnetization with an applied magnetic field $H = 200$ Oe under ZFC and FC protocols together with the heat capacity for the SC1R single crystal is depicted in Fig. 3. The ZFC and FC magnetization curves follow similar behaviour as in its powder counterpart. However the heat capacity curve $C_P(T)$ shows at $T_{\mathrm{N}} = 41$ K an anomaly, that corresponds well with the FIM transition temperature, followed by two sharp peaks at $T_{\mathrm{I1}} = 20$ K and $T_{\mathrm{I2}} = 18$ K, signalling that two phase transitions take place at these temperatures. Heat capacity curves for $MnCr_2O_4$ synthesized under air conditions reported by other authors [23, 35, 44] only developed a single anomaly at low temperatures. For temperatures below T_{N}, it is noticeable the different behaviour of the magnetization and heat capacity curves depending on the atmosphere under which the sample was synthesized.

B. NPD experiments

Some representative powder diffraction patterns collected between 1.6 K and 300 K are shown in Fig. 4 for all samples. In this section we will focus in a qualitative analysis of these patterns and for that reason only the low-Q part is plotted.

The first remarkable issue is the presence of an impurity phase for the oxidizing samples, S1A and S2A, which is clearly visible as a reflection at $Q = 1.74$ Å^{-1} detectable at all the temperatures with constant intensity. These reflections are showed in Fig. 4 (c) and (d) with an asterisk. In the next section we will see that this impurity correspond with Cr_2O_3 and amounts for around 3%.

In all four samples it is possible to observe an increase in the intensity of the reflection at $Q = 2.1$ Å^{-1} below $T_{\mathrm{N}} \sim 40$ K. This is related with the phase transition from the paramagnetic state to an ordered magnetic state with propagation vector $\vec{k}_{\mathrm{N}}$=(0 0 0) and it is associated to the ferrimagnetic state already reported. Also a bump in the background around $Q = 1.46$ Å^{-1} for temperatures in the vicinity of $T_{\mathrm{I1}} \gtrsim 20$ K is observed in all the samples. This bump is related with some magnetic SRO that anticipates the appearance of a set of new satellite reflections, indexed with an incommensurate propagation vector $\vec{k}_{\mathrm{I1}} = (\delta\, \delta\, 0)$, for $T \lesssim T_{\mathrm{I1}} = 20$ K. This propagation vector is in agreement with other NPD experiments done in $MnCr_2O_4$ [12, 29, 34, 36]. In Fig. 4 the satellite reflections associated to $\vec{k}_{\mathrm{I1}}$ are signalled with red symbols (asterisk and circles) for each sample.

For sample S1R (Fig. 4 (a)), a different set of satellite reflections develops for $T \lesssim T_{\mathrm{I2}} = 18$ K, being the new incommensurate propagation vector $\vec{k}_{\mathrm{I2}} = (\alpha\, \beta\, \gamma)$. For this sample, at these temperatures, the simultaneous presence of $\vec{k}_{\mathrm{I1}}$ and $\vec{k}_{\mathrm{I2}}$ vectors is not detected. However, for sample S2R (Fig. 4 (b)) the same propagation vector $\vec{k}_{\mathrm{I2}}$ appears for $T \lesssim T_{\mathrm{I2}} = 18$ K but some reminiscence of the reflections coming from $\vec{k}_{\mathrm{I1}}$ still survive until the lowest measured temperatures. Satellite reflections due to the $\vec{k}_{\mathrm{I2}}$ propagation vector are shown with blue symbols (asterisks and circles) in Fig. 4.

The diffractograms for S1A (Fig. 4(c)) collected at $T \lesssim T_{\mathrm{I1}} = 19$ K show reflections which can all be indexed with a unique $\vec{k}_{\mathrm{I1}}$ till the lowest measured temperature. For the sample S2A (Fig. 4 (d)) at $T \lesssim T_{\mathrm{I1}} = 19$ K, also both propagation vectors survive but in this sample the minority phase correspond to $\vec{k}_{\mathrm{I2}}$.

The evolution with the temperature of the intensity for the (2 2 0) nuclear reflection, which also has a magnetic contribution indexed with $\vec{k}_{\mathrm{N}}$ (in black), the satellite (0 0 2) + $\vec{k}_{\mathrm{I1}}$ (in red) and the satellite (1 $\bar{1}$ 1) + $\vec{k}_{\mathrm{I2}}$ (in blue) for the different samples is shown in Fig. 5. For samples S1R and S2R we clearly observe a sharp decrease in the intensity for the reflection (2 2 0) at $T_{\mathrm{I2}} = 18$ K, when the new $\vec{k}_{\mathrm{I2}}$ propagation vector appears. However, in sample S1A or S2A no sharp decrease in the (2 2 0) nuclear reflection intensity is observed because the new $\vec{k}_{\mathrm{I2}}$ does not appear, like in S1A, or its intensity is small, like in S2A, and therefore its relative effect in the high intensity (2 2 0) line is imperceptible. The evolution of these intensities together with Fig. 4 allows to quantitatively distinguish between the different magnetic phases that are present, as will be discussed later in section V B.

IV. ANALYSIS OF THE NPD EXPERIMENTS

In this section the Rietveld refinement and symmetry analysis of the diffractograms collected for all the samples at different temperatures will be presented in detail. For it, different tools were used, which include the FullProf Suite [45], the ISODISTORT Suite [46, 47] and several utilities within the Bilbao Crystallographic Server [48–51]. The magnetic superspace group (MSSG) formalism [39–41] will be employed to describe the different magnetic and nuclear structures.

A. Paramagnetic Phase

The diffractograms at room temperature for all the samples were refined within the magnetic space group (MSG) $Fd\bar{3}m.1'$ in which the Mn, Cr and the O occupy, respectively, the Wyckoff positions (WP) 8a, 16d and 32e. Moreover for samples synthesized in oxidizing atmosphere (S1A and S2A) an impurity phase of Cr_2O_3, with structural parameters given by ref. [52], was refined to account for some extra peaks. For samples S1R and S2R, the impurity was not detected.

An improvement in the refinements for samples S1A and S2A was made by supposing that there is a relatively

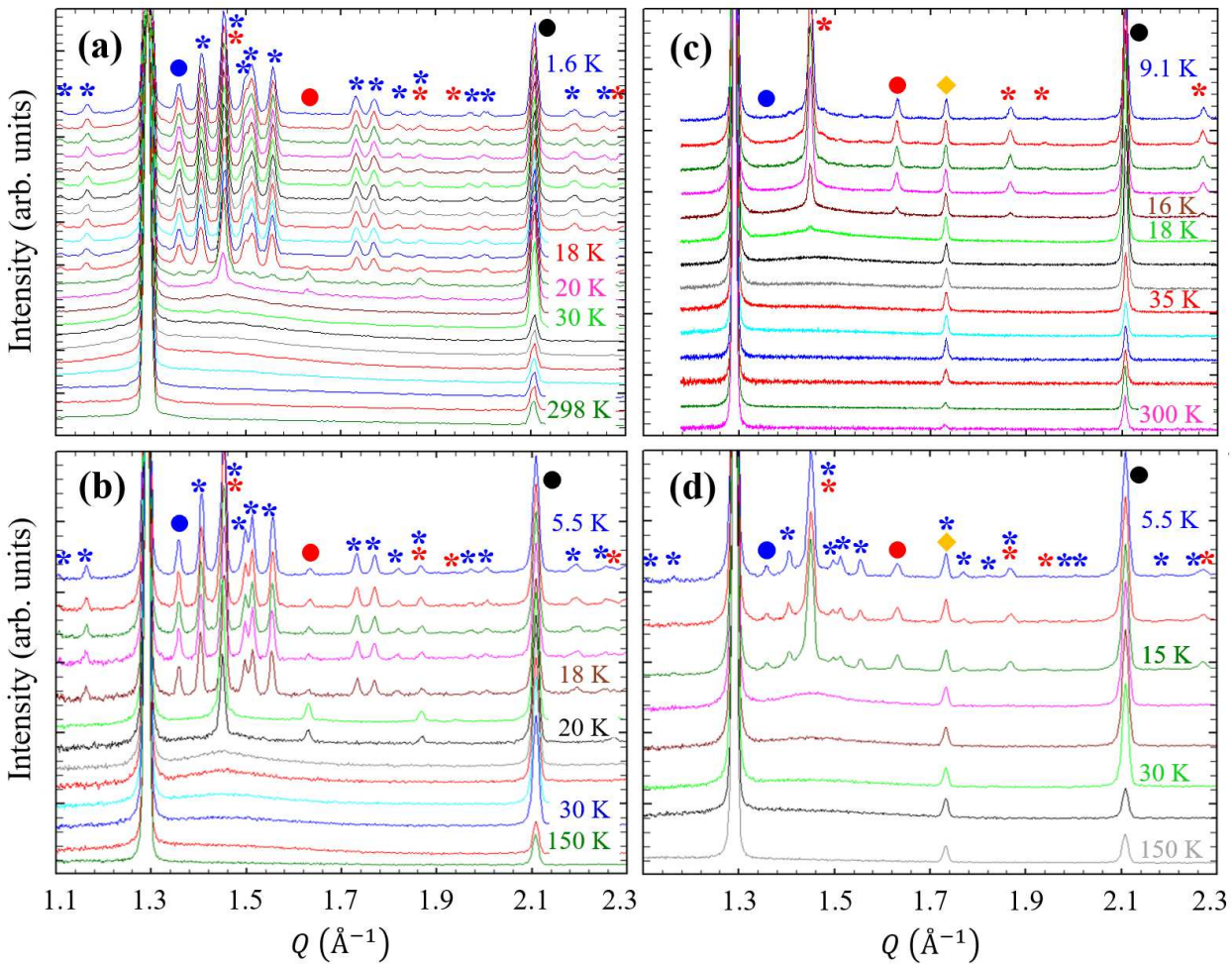

FIG. 4. Low Q part of diffraction patterns obtained at different temperatures for S1R sample at G.4.1 (a), S2R sample measured at NOVA (b), S1A sample at S-HRPD (c), and S2A sample at NOVA (d). Reflections due to the Cr_2O_3 impurity in (c) and (d) are labelled with a yellow diamond. The satellite reflections due to $\vec{k}_{I1}$ and $\vec{k}_{I2}$ are, respectively, indicated in the upper part of each figure with red and blue symbols (asterisk and circles). The reflections mentioned in Fig. 5, $(2\,2\,0)+\vec{k}_N$, $(0\,0\,2)+\vec{k}_{I1}$, and $(1\,\bar{1}\,1)+\vec{k}_{I2}$ are, respectively, marked with black, red and blue circles.

small defect, ϵ, of Mn^{2+} replacing the lack of Cr^{3+} on the B-sites. Since they were synthesized under air, we can suppose that a reaction like the following takes place in the synthesis process:

$$MnO + Cr_2O_3 + \tfrac{3}{2}\epsilon\, O_2 \rightarrow Mn_{1-2\epsilon}\,[Mn_\epsilon Cr_{1-\epsilon}]_2\, O_4 + \epsilon\, Cr_2O_3$$

where the excess ϵ of O_2 (from the air) produces the impurity phase. No improvement was made by refining the occupancy of the O^{2-} ions, which suggests that no oxygen diffusion process takes place. At these temperatures, the main free structural parameters refined for $MnCr_2O_4$ were the lattice parameter a and the atomic position x of the O atom, which were in good agreement with ref. [25]. The amount ϵ of Mn detected at the site 16d was 0.19(2) and 0.07(5) for, respectively, S1A and S2A. The weight percentage of impurity was 2.94(5)% for S1A and 3(1)% for S2A. All these parameters are listed in Table I for the sample S1A.

It was considered that the amount of the impurity phase determined in the paramagnetic phase is keep constant in the subsequent refinements done for each sample (S1A and S2A) at lower temperatures. Moreover, when the symmetry decreased, and therefore the WP split, as lowering the temperature, the occupancy ϵ of Mn at the site of the Cr 16d has been considered homogeneously shared among the new WP (e.g. 4b and 4d at $Imm'a'$ at $T = 35$ K).

B. (0 0 0) - Ferrimagnetic Phase

As the temperature decreases below 298 K, the diffraction patterns show no substantial changes. However, depending on each particular sample, below $\sim$ 41 K a mag-

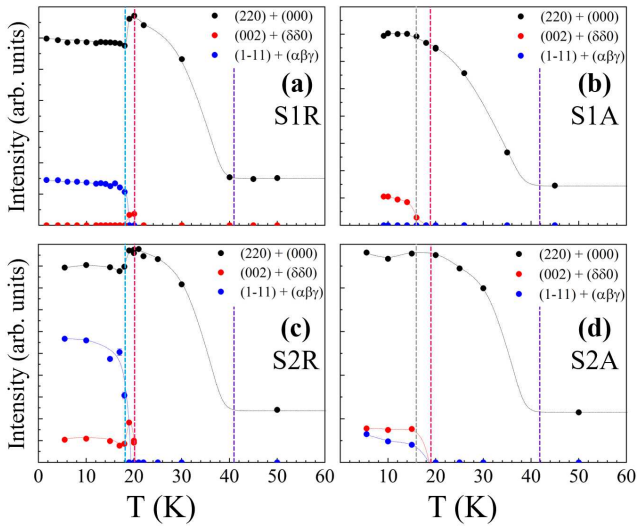

FIG. 5. Evolution with temperature of the intensity of some magnetic reflections; $(2\,2\,0)+\vec{k}_{\rm N}$ in black, $(0\,0\,2)+\vec{k}_{\rm I1}$ in red and $(1\,\bar{1}\,1)+\vec{k}_{\rm I2}$ in blue for each sample. The transition temperatures determined from the magnetization measurements $T_{\rm N}$, $T_{\rm I1}$, $T_{\rm I2}$ and $T_{\rm L}$ are showed with purple, blue, pink and grey lines.

netic intensity appear superimposed with some nuclear Bragg reflections indicating the presence of a $\vec{k}_{\rm N}=(0\,0\,0)$ propagation vector. This behaviour is common to all the four samples.

As mentioned before, the paramagnetic structure is described by the $Fd\bar{3}m.1'$ MSG, regardless of the impurity presence. Using Irreducible Representations concepts, we can decompose the magnetic representation for each of the WP 8*a* and 16*d* as direct sum of Irreducible Representations (*irreps*) of $Fd\bar{3}m.1'$, which is the little group of $\vec{k}_{\rm N}=(0\,0\,0)$, as follows:

$$\mathrm{m}\Gamma_{8a} = 1\mathbf{m\Gamma_4^+(3)} \oplus 1\mathrm{m}\Gamma_5^-(3)$$
$$\mathrm{m}\Gamma_{16d} = 1\mathrm{m}\Gamma_2^+(1) \oplus 1\mathrm{m}\Gamma_3^+(2) \oplus 2\mathbf{m\Gamma_4^+(3)} \oplus 1\mathrm{m}\Gamma_5^+(3)$$

which shows that the common *irrep* for both sites is $\mathrm{m}\Gamma_4^+(3)$, according the notation of the Bilbao Crystallographic Server (BCS) [48–51]. This magnetic order could be described by 9 free parameters, 6 for the Cr site and 3 for the Mn one.

In order to obtain more information about the real symmetry of this magnetic phase we employed the k-SUBGROUPSMAG tool of the BCS which provides with the isotropy subgroups of the parent group $Fd\bar{3}m.1'$ that are compatible with the $\mathrm{m}\Gamma_4^+(3)$ as a primary *irrep*. Following this procedure 6 isotropy subgroups appeared ($R\bar{3}m'$, $I4_1/am'd'$, $Imm'a'$, $C2'/c'$, $C2'/m'$ and $P\bar{1}$) each of them with a different order parameter direction. For each one of them we split the parent WP for Mn(8*a*), Cr(16*d*) and O(32*e*) accordingly to the lower symmetry of each isotropy subgroup.

TABLE I. Structural refinement for sample S1A at $T=298$, 30 and 9.1 K obtained from the patterns collected at S-HRPD. The forth column (I_1^*) shows the results obtained considering the values that reproduce the parent WP as fixed parameters (i.e. $u=0.73593(2)$).

	S1A: S-HRPD			
Phase	PM	FIM	I_1	I_1^*
T (K)	298	20	9.1	9.1
MSSG	$Fd\bar{3}m.1'$	$Imm'a'$	$Im'a'2(0\,0\,\gamma)0ss$	$Im'a'2(0\,0\,\gamma)0ss$
#	227.129	74.559	46.1.12.4.m245.1	46.1.12.4.m245.1
$\vec{k}$		(0 0 0)	(δ δ 0)	(δ δ 0)
δ			0.62730(5)	0.62725(5)
irreps		$\mathrm{m}\Gamma_4^+(3)$	$\mathrm{m}\Gamma_4^+(3)\oplus\mathrm{m}\Sigma_2(1)$	$\mathrm{m}\Gamma_4^+(3)\oplus\mathrm{m}\Sigma_2(1)$
a (Å)	8.43673(1)	5.96069(1)	5.96062(2)	5.96061(2)
b (Å)		5.96069(1)	8.42567(5)	8.42568(5)
c (Å)		8.42566(4)	5.96062(2)	5.96061(2)
Mn	$8a(\frac{1}{8}\ \frac{1}{8}\ \frac{1}{8})$	$4e(0\ \frac{1}{4}\ z)$	$4b(\frac{1}{4}\ y\ z)$	$4b(\frac{1}{4}\ y\ z)$
y			0.88(1)	0.875
z		0.128(1)	0.0(1)	0.000
Cr	$16d(\frac{1}{2}\ \frac{1}{2}\ \frac{1}{2})$	$4b(0\ 0\ \frac{1}{2})$	$4a(0\ 0\ z)$	$4a(0\ 0\ z)$
z			0.5(1)	0.500
		$4d(\frac{1}{4}\ \frac{3}{4}\ \frac{1}{4})$	$4b(\frac{1}{4}\ y\ z)$	$4b(\frac{1}{4}\ y\ z)$
y			0.250(6)	0.250
z			0.2(1)	0.250
O	$32e(u\ u\ u)$	$8h(0\ y\ z)$	$8c(x\ y\ z)$	$8c(x\ y\ z)$
u , x	0.73593(2)		0.527(5)	$0.528=-2u$
y		0.476(2)	0.735(4)	$0.736=u$
z		0.736(1)	0.0(1)	0.000
		$8i(x\ \frac{1}{4}\ z)$	$4b(\frac{1}{4}\ y\ z)$	$4b(\frac{1}{4}\ y\ z)$
x		0.222(2)		
y			0.486(5)	$0.486=u-\frac{1}{4}$
z		0.515(1)	0.8(1)	$0.778=-2u-\frac{3}{4}$
			$4b(\frac{1}{4}\ y\ z)$	$4b(\frac{1}{4}\ y\ z)$
y			0.015(4)	$0.014=-u-\frac{1}{4}$
z			0.7(1)	$0.722=2u-\frac{3}{4}$
ϵ Mn(16*d*)	0.19(2)	0.19	0.19	0.19
% wgt. Cr_2O_3	2.94(5)	2.94	2.94	2.94
$\mathrm{R}_{\rm Bragg}$	1.74	4.30	4.11	4.17

We were successful at fitting the data of this phase, in all the samples, with the centrosymmetric magnetic subgroup $Imm'a'$, which allows an order parameter direction along $\langle a\ \bar{a}\ 0\rangle$. In this case the parent Mn(8*a*), Cr(16*d*) and O(32*e*) became Mn(4*e*), Cr(4*b*), Cr(4*d*), O(8*h*) and O(8*i*) in the new MSG. The results of our Rietveld refinement of the S-HRPD diffractograms for S1A at 20 K are listed in the second column of Table I and show that the tetragonal structure is a quasi cubic one. Fig. 6 shows the evolution of the lattice parameters with temperature for samples S1R and S1A. The values are referred to the standard setting of the paramagnetic group. Table I shows the atomic coordinates in the standard setting of each MSG. In this magnetic structure the magnetic moments of each Cr and Mn sub-lattices order ferromagnetically along the $\langle 1\ \bar{1}\ 0\rangle$ axis and are coupled antiferromagnetically, in accordance with the results from previous studies [12, 19, 29, 34, 36, 37, 53].

TABLE II. Structural and magnetic refinement for sample S1R at $T = 298$, 30, 20 and 1.6 K obtained from the patterns collected at G.4.1. The atomic coordinates, lattice parameters and magnetic moments are referred to the standard setting of the paramagnetic group.

	S1R: G.4.1			
Phase	PM	FIM	I_1	I_2
T (K)	298	30	20	1.6
MSSG	$Fd\bar{3}m.1'$	$Imm'a'$	$Im'a'2(0\ 0\ \gamma)0ss$	$P1(\alpha\ \beta\ \gamma)0$
#	227.129	74.559	46.1.12.4.m245.1	1.1.1.1.m1.1
$\vec{k}$		(0 0 0)	$(\delta\ \delta\ 0)$	$(\alpha\ \beta\ \gamma)$
δ , α			0.6233(4)	0.6597(1)
β				0.5999(1)
γ				0.1996(2)
irreps		$m\Gamma_4^+(3)$	$m\Gamma_4^+(3) \oplus m\Sigma_2(1)$	$m\Gamma_4^+(3) \oplus mG_1(1)$
a (Å)	8.4355(2)	8.4297(6)	8.4297(5)	8.4271(7)
b (Å)		8.4297(6)	8.4297(5)	8.4306(2)
c (Å)		8.426(1)	8.425(1)	8.426(7)
$\vec{M}_0$		$\langle 1\ \bar{1}\ 0 \rangle$	$\langle 1\ \bar{1}\ 0 \rangle$	$\langle 1\ 0\ 0 \rangle$
$\vec{M}_s$			$\langle 1\ 1\ 0 \rangle$	$\langle 0\ 0\ 1 \rangle$
$\vec{M}_c$			$\langle 0\ 0\ 1 \rangle$	$\langle 0\ 1\ 0 \rangle$
Mn	$8a(\frac{1}{8}\ \frac{1}{8}\ \frac{1}{8})$	$8e(\frac{1}{8}\ \frac{1}{8}\ \frac{1}{8})$	$8b(\frac{1}{8}\ \frac{1}{8}\ \frac{1}{8})$	$4a(\frac{1}{8}\ \frac{1}{8}\ \frac{1}{8})$
$M_0(\mu_B)$		-2.92(3)	-3.35(3)	-3.11(4)
$M_s = M_c(\mu_B)$			0.88(8)	2.8(2)
				$4a(\frac{7}{8}\ \frac{7}{8}\ \frac{7}{8})$
$M_0(\mu_B)$				-3.11(4)
$M_s = M_c(\mu_B)$				2.8(1)
Cr	$16d(\frac{1}{2}\ \frac{1}{2}\ \frac{1}{2})$	$8d(\frac{1}{2}\ \frac{1}{2}\ \frac{1}{2})$	$8b(\frac{1}{2}\ \frac{1}{2}\ \frac{1}{2})$	$4a(\frac{1}{2}\ \frac{1}{2}\ \frac{1}{2})$
$M_0(\mu_B)$		1.20(8)	1.35(7)	1.12(7)
$M_s = M_c(\mu_B)$			0.88(3)	3.43(7)
				$4a(\frac{1}{4}\ \frac{3}{4}\ 0)$
$M_0(\mu_B)$				1.12(7)
$M_s = M_c(\mu_B)$				2.24(7)
		$8b(\frac{3}{4}\ 0\ \frac{1}{4})$	$8a(\frac{3}{4}\ 0\ \frac{1}{4})$	$4a(\frac{3}{4}\ 0\ \frac{1}{4})$
$M_0(\mu_B)$		1.00(4)	1.15(4)	1.03(6)
$M_s = M_c(\mu_B)$			0.42(8)	0.66(8)
				$4a(0\ \frac{3}{4}\ \frac{1}{4})$
$M_0(\mu_B)$				1.03(6)
$M_s = M_c(\mu_B)$				1.58(8)
R_{Bragg}	0.696	0.627	1.17	1.62
R_{Bragg} (Mag.)		1.80	3.94	3.22

The observed and calculated diffractograms for selected temperatures of S1R, emphasizing the low Q part where magnetic signals are more visible, are depicted in Fig. 7 and the numerical values for the magnetic moments obtained from such refinements in sample S1R are also listed in the Table II, where the atomic coordinates, lattice parameters and magnetic moments are referred to the standard setting of the paramagnetic group. For all the samples these values are similar.

A schema of the (0 0 0) - FIM phase happening in all the samples can be found in Fig. 9.

C. $(\delta\ \delta\ 0)$ - Incommensurate Phase

As decreasing the temperature below T_{I1}=20 K, for the reduced samples, and T_{I1} = 19 K for the oxidized ones, new magnetic satellite reflections, indexed with a incommensurate propagation vector $\vec{k}_{I1} = (0.6233(4)\, 0.6233(4)\, 0)$, the same for all the samples, appear. However the magnetic contribution at the nuclear Bragg reflections indexed with $\vec{k}_N = (0\,0\,0)$ is still present and it even continues increasing. This can be observed in Fig. 5.

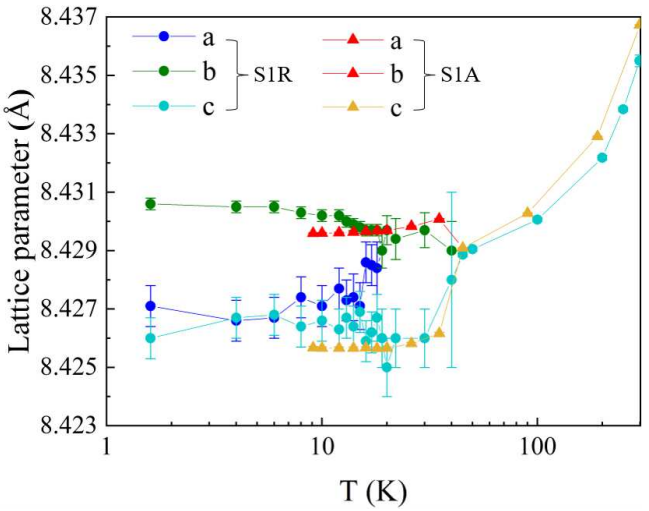

FIG. 6. Temperature-dependent changes in the lattice parameters for samples S1R and S1A. To enable easy comparison at lower temperature values, the temperature axis is presented on a logarithmic scale. The lattice parameters are referred to the standard setting of the paramagnetic group.

Thus, the magnetic structure in this phase is described by two *irreps* at least, one for each propagation vector. In this case the decomposition of the magnetic representation of the space group $Fd\bar{3}m.1'$ and $\vec{k}_{I1} = (\delta\ \delta\ 0)$, with $\delta = 0.6233(4)$, for the WP $8a$ and $16d$ shows that the same four 1-d *irreps* are present at both sites according to:

$$m\Gamma_{8a} = 1m\Sigma_1(1) \oplus 2m\Sigma_2(1) \oplus 1m\Sigma_3(1) \oplus 2m\Sigma_4(1)$$
$$m\Gamma_{16d} = 2m\Sigma_1(1) \oplus 4m\Sigma_2(1) \oplus 3m\Sigma_3(1) \oplus 3m\Sigma_4(1)$$

Therefore, the irreducible representations theory, does not help to restrict the number of free parameters to unambiguously describe the magnetic structure.

In this magnetic phase it is not possible to use the Shubnikov magnetic groups, since the propagation vector implies an incommensurate structure, but we have to make use of the magnetic superspace group (MSSG) formalism [39–41].

In this general formalism, the magnetic structure is described by a basic structure, related to the nuclear paramagnetic cell, in addition to a series of d-magnetic modulation functions with propagation vector $\vec{k}_i$, and its n-harmonics, that describes the variation from the basic structure of the magnetic moments. These modulations are given by additional internal coordinates x_{3+i}

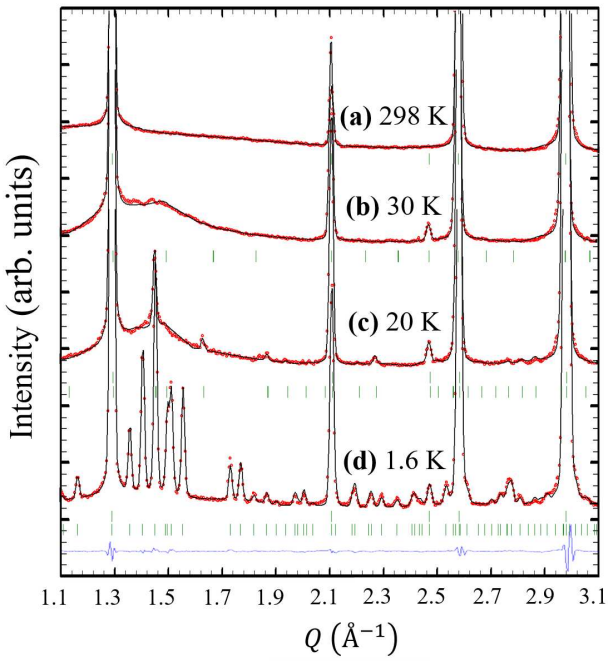

FIG. 7. Representative Rietveld refinements at selected temperatures for sample S1R. In red are shown the observed points and in back continuous line the calculated pattern with the parameters shown in Table II. The blue continuous line and the green ticks indicate the difference between the observed and calculated profile and the nuclear and satellite peaks generated by the magnetic superspace group, respectively.

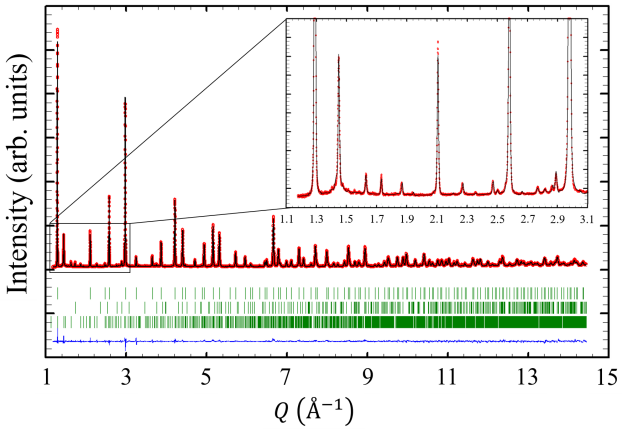

FIG. 8. High resolution diffractogram collected at $T = 9.1$ K for sample S1A at the instrument S-HRPD. In red are shown the observed points and in back continuous line the calculated pattern with the parameters shown in Table I. The blue continuous line and the green ticks indicate the difference between the observed and calculated profile and the nuclear and satellite peaks generated by the magnetic superspace group, respectively. The insert shows a zoom of the low-Q part, where the scale is the same as in Fig. 7.

$(i = 1, 2...d)$, one for each propagation vector, where $x_{3+i} = (\vec{k}_i \cdot \vec{r}_{lj})$ and $\vec{r}_{lj}$ represents the position of atom j in the l-th unit cell. If we consider only one propagation vector, then the magnetization $\vec{M}_{lj}$ can be expressed in a real Fourier series as:

$$\vec{M}_{lj} = \vec{M}_{j,0} + \\ + \sum_{n=1}^{\infty} \left[\vec{M}^n_{j,\mathrm{s}} \sin(2\pi n x_4) + \vec{M}^n_{j,\mathrm{c}} \cos(2\pi n x_4) \right] \quad (2)$$

In our case, the sum has one term ($n = 1$) because of the presence of only one propagation vector $\vec{k}_{\mathrm{I1}}$, with only one harmonic, so Eq. 2 reads

$$\vec{M}_{lj} = \vec{M}_{j,0} + \vec{M}_{j,\mathrm{s}} \sin(2\pi x_4) + \vec{M}_{j,\mathrm{c}} \cos(2\pi x_4)$$

where $x_4 = \vec{k}_{\mathrm{I1}} \cdot \vec{r}_{lj}$. The sine and cosine modulation waves $\vec{M}_{j,\mathrm{c}} \cos(2\pi x_4)$ and $\vec{M}_{j,\mathrm{s}} \sin(2\pi x_4)$ must comply with the symmetry constraints imposed by the MSSG. This formalism has been very recently implemented in FULLPROF [45], in combination with the ISOTROPY suite [46] to allow for the refinement of neutron diffraction data.

Several MSSGs are compatible with the combination between $Fd\bar{3}m.1'$ and magnetic distortions for the Mn and Cr atoms, given by 2 superposed *irreps*: m$\Gamma_4^+(3)$ for the propagation vector $\vec{k}_{\mathrm{N}} = (0\,0\,0)$ (Γ point) and depending on the irreducible magnetic representation chosen for $\vec{k}_{\mathrm{I1}} = (\delta\,\delta\,0)$, ($\Sigma$ point). From all the possible isotropy subgroups, we focused our analysis on the ones described by the *irrep* m$\Gamma_4^+(3)$ with the order parameter direction along $\langle a\ \bar{a}\ 0 \rangle$.

After a systematic analysis by trial and error, the best fit, shown in Fig. 7(c), was obtained for the non-centrosymmetric $Im'a'2(0\,0\,\gamma)0ss$ MSSG, described by a combination of the *irreps* m$\Gamma_4^+(3)$ and m$\Sigma_2(1)$. Similarly to the $\vec{k}_{\mathrm{N}}$-FIM phase, the nuclear structure of this MSSG is a tetragonal one, and the WP are further split from Mn($4e$), Cr($4b$), Cr($4d$), O($8h$) and O($8i$) in FIM-phase to Mn($4b$), Cr($4a$), Cr($4b$), O($8c$), O($4b$) and O($4b$) in the new I$_1$-phase. The quality of the refinement can be appreciated in the Fig. 8, where the full diffractogram measured in S-HRPD for S1A at $T = 9.1$ K is shown together with the Rietveld fit and the difference between the calculated and observed profiles. The results of the Rietveld refinement for S1A at 9.1 K can be found in the third column of Table I. A comparison with the fourth column of Table I, in which the values that reproduce the parent WP were fixed (i.e. $u = 0.73593(2)$), shows that the tetragonal distortions are practically negligible.

Regarding the magnetic structure of this phase, the Cr and Mn sublattices remain coupled antiferromagnetically with a net magnetic moment $\vec{M}_{j,0}$ pointing along $\langle 1\,\bar{1}\,0 \rangle$, while the propagation vector $\vec{k}_{\mathrm{I1}}$ induces a cycloidal order where the modulated components $\vec{M}_{j,\mathrm{c}}$ and $\vec{M}_{j,\mathrm{s}}$ are in the plane perpendicular to $\langle 1\,\bar{1}\,0 \rangle$. The magnetic pa-

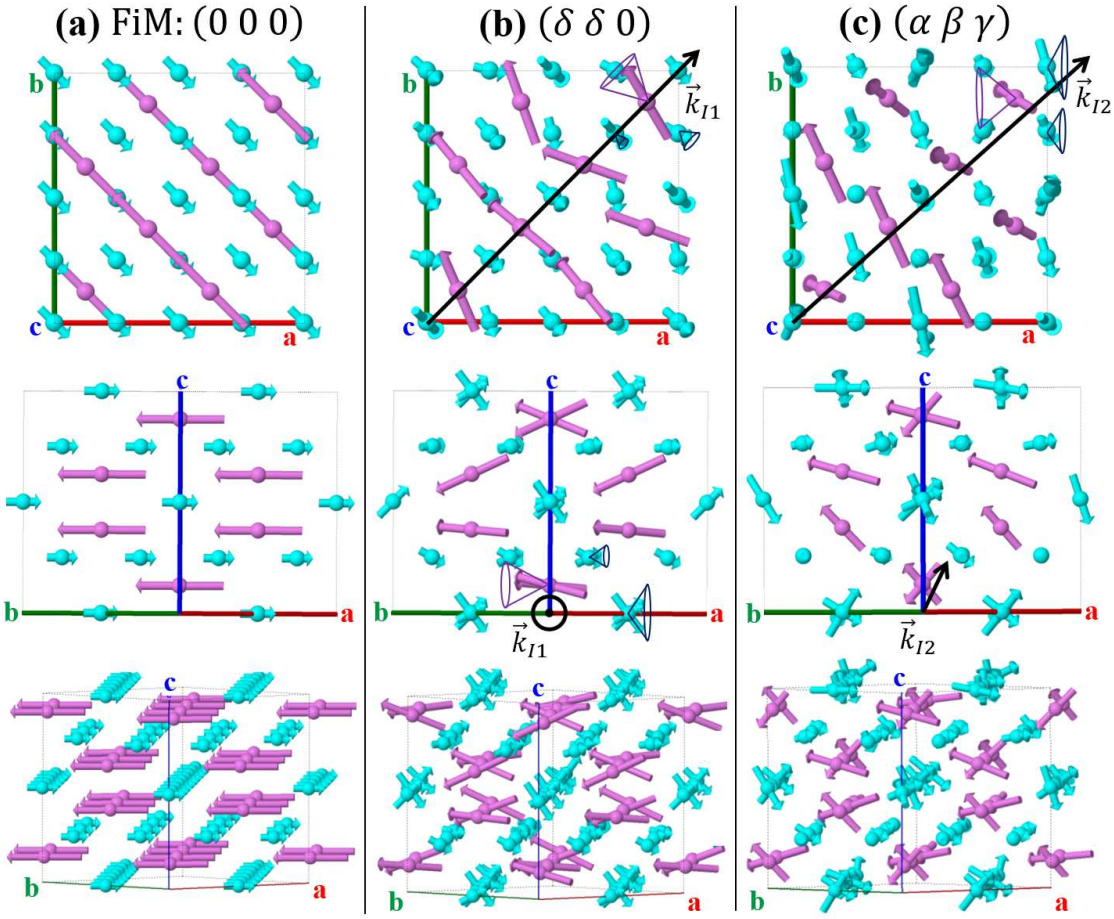

FIG. 9. Views of the magnetic structures determined for each phase, a) (0 0 0), b) (δ δ 0) and c) (α β γ).

rameters of the $Im'a'2(0\,0\,\gamma)0ss$ MSSG obtained from the refinements in sample S1R are listed in the third column of Table II. The amplitude of the modulation waves $\vec{M}_{j,c}$, $\vec{M}_{j,s}$ was constrained to the same value, since no improvement in the refinement was observed if they acted as independent parameters.

A schema of the (δ δ 0) - Incommensurate phase happening in all the samples can be found in Fig. 9(b).

D. (α β γ) - Incommensurate Phase

For the sample S1R, a different set of satellite reflections appear below T_{I2}=18 K which are indexed with the incommensurate propagation vector $\vec{k}_{I2}$ = (0.6597(1) 0.5999(1) 0.1996(2)). For this phase the magnetic contribution at the nuclear Bragg reflections ($\vec{k}_N$ = (0 0 0)) is also present, although its intensity slightly decreases, as can be observed in Fig. 5. As it was previously mentioned, for S1A no satellite reflections which could be indexed with $\vec{k}_{I2}$ were found down to the lowest temperature measured. Meanwhile, all $\vec{k}_N$, $\vec{k}_{I1}$ and $\vec{k}_{I2}$ vectors are detected below T_{I2}=18 K and T_{I2}=19 K, for, respectively, samples S2R and S2A (see Fig. 5). The simultaneous presence of $\vec{k}_{I1}$ and $\vec{k}_{I2}$ in these samples suggests the existence of micro-crystallites with different magnetic ordering.

The magnetic structure in this phase is also described by two *irreps*. The decomposition of the magnetic representation of space group $Fd\bar{3}m.1'$ and $\vec{k}_{I2}$ for the WP 8*a* and 16*d* gives mΓ_{8a} = 6m$\mathcal{K}(1)$ and mΓ_{16d} = 12m$\mathcal{K}(1)$, where the 1-d-*irrep* m$\mathcal{K}(1)$ stands for a general point of the Brillouin Zone. Nevertheless, the *irrep* m$\mathcal{K}(1)$ does not impose any constraint to the symmetry of the magnetic structure, which can be described by 18 free parameters, 12 for the Cr site and 6 for the Mn one.

Two MSSGs are compatible with the combination between the MSG $Fd\bar{3}m.1'$ and magnetic distortions for the Mn and Cr atoms, given by 2 superposed *irreps*: $m\Gamma_4^+(3)$ for the propagation vector $\vec{k}_N$ (Γ point) and m$\mathcal{K}(1)$ for $\vec{k}_{I2}$ = ($\alpha\,\beta\,\gamma$) ($\mathcal{K}$-General Point). However, only in the case of the non-centrosymmetric $P1(\alpha\,\beta\,\gamma)0$ MSSG a good fit is obtained, as can be observed in Fig. 7d).

At this point the only symmetry operations that re-

main for the nuclear structure are the centring of the faces, which implies that the WP are further split to $4a$ for all the atoms (see Table II). Although the nuclear space group is triclinic, only the cell parameters were fitted independently, since no improvement in the refinement was observed if the cell angles were allowed to vary from 90°. In fact the deviation of the cell parameters respect the cubic case is quasi imperceptible, as can be read from Table II.

The magnetic structure described by the $P1(\alpha\,\beta\,\gamma)0$ MSSG is also a transverse conical ferrimagnetic structure, but the net magnetic moment $\vec{M}_{j,0}$ is reoriented along $\langle 1\,0\,0\rangle$, while the modulated components $\vec{M}_{j,\mathrm{c}}$ and $\vec{M}_{j,\mathrm{s}}$ of the propagation vector $\vec{k}_{\mathrm{I2}}$ remain in the yz plane.

In the same way as in the previous $(\delta\,\delta\,0)$ phase, the amplitude of the modulation waves $\vec{M}_{j,\mathrm{c}}$, $\vec{M}_{j,\mathrm{s}}$ was constrained to the same value, since no improvement in the refinement was observed relaxing this constraint. Also the values of $\vec{M}_{j,0}$ were constrained to be the same for the split atoms that belonged to the same WP in the $Imm'a'$ MSG. The nuclear and magnetic parameters obtained from the refinements in sample S1R are listed in the fourth column of Table II.

A schema of the $(\alpha\ \beta\ \gamma)$ - Incommensurate phase happening in S1R, S2R and S2A samples can be found in Fig. 9(c).

V. DISCUSSION

A. Temperature evolution

Fig. 10 (a), (b) and (c) show the evolution of the magnetic moment modulus M_j, the half-cone angle α and the net magnetic moment $M_{j,0}$, respectively, extracted from the Rietveld analysis of sample S1R. A visual representation of these parameters is depicted inside Fig. 10 (b). The number in the name of each j atom follows the order of appearance in Table II.

Below $T_{\mathrm{N}} \sim 41$ K, where the $\vec{k}_{\mathrm{N}} = (0\,0\,0)$ ferrimagnetic phase is developed, M_j and $M_{j,0}$ are equivalent, and an increase in these values followed by a plateau is observed. The split in the WP of Cr is easily observed in Fig. 10 (a) and (c), since one of the Cr sublattices (B1: Cr1 and Cr2) has a slightly higher value than the other one (B2: Cr3 and Cr4). Below $T_{\mathrm{I1}} = 20$ K, $\vec{M}_{j,0}$ remains at almost the same value as in the previous phase. However, a sudden increase for all the atoms in both the magnetic moment modulus M_j and the half-cone angle α signals the development of a conical magnetic structure in the $(\delta\,\delta\,0)$ phase (see Fig. 10 (a) and (b)).

The half-cone angle values obtained at 20 K for the A, B1 and B2 sublattices are, respectively, 26°, 41° and 34°. Previous works reported for the same set of angles the values; 24°, 62°, 14° [29] and 28°, 85°, 11° [12]. However, in those studies the magnetic moment of both Mn^{2+} and Cr^{3+} was fixed to its spin-only value, and in this work it were consider as fitting parameters.

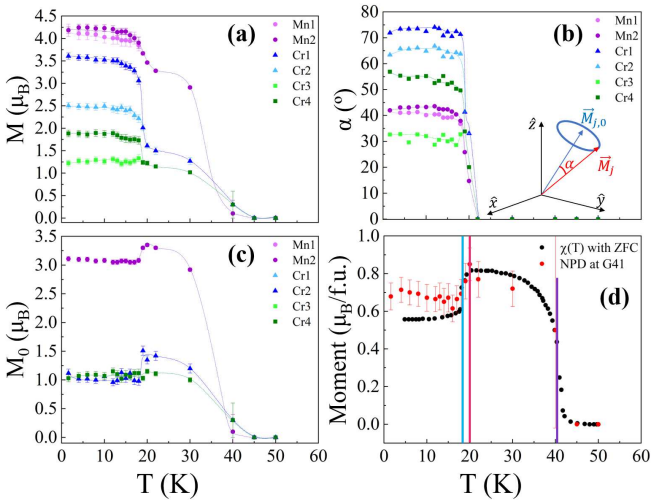

FIG. 10. Temperature evolution of the parameters defining the magnetic structures: M_j (a), α (b), $M_{j,0}$ (c) extracted from the Rietveld analysis of sample S1R. A comparison between the magnetization obtained from the fits to the NPD data (red) and the susceptibility measured at ZFC (black) is shown in (d).

Below $T_{\mathrm{I2}} = 18$ K the $(\alpha\,\beta\,\gamma)$ phase is developed, and the Mn are split into 2 different sublattices, which display a nearly identical behaviour (see Fig. 10 (a) and Fig. 10 (b)). Meanwhile, the 2 Cr sublattices are further split into 4, and in both cases the split is divided into a sublattice with values for M_j and α that follow the previous tendency (Cr2 and Cr3), and another sublattice with a steep increase for these values (Cr1 and Cr4). As the temperature is decreased, all the sublattices values remain constant down to the lowest temperature measured. The saturation value for the Mn^{2+} is close to the calculated value of 4.3 μ_{B} [36], while in the B-sublattices none of the Cr^{3+} ions reach its theoretical saturation value of 3.87 μ_{B}. As it was mentioned before, the values of $\vec{M}_{j,0}$ in the $(\alpha\,\beta\,\gamma)$ phase were constrained to be the same for the split atoms that belonged to the same WP in the $Imm'a'$ MSG. A small decrease in $\vec{M}_{j,0}$ can be observed in Fig. 10 (c), in agreement with the evolution of the nuclear intensities observed in Fig. 5 (a).

By plotting the component of the net magnetic moment $M_{j,0}$ which is parallel to the $\langle 1\,\bar{1}\,0\rangle$ direction, a good agreement is observed between the values obtained from the analysis of the NPD data and the net magnetization calculated from the ZFC susceptibility, which is shown in Fig. 10 (d).

B. Sample dependence

Taking into account both the results from the magnetization and heat capacity experiments and the analysis of

the NPD experiments, a summary of the magnetic phases that are observed in each sample is presented in Fig. 11. The differences observed in the transition temperatures of these phases suggest a strong dependence between the magnetic ground state and the atmosphere in which the samples were synthesized. This idea was already pointed out in ref. [32, 54]. In particular, it seems that the synthesis of a sample under an oxidizing atmosphere prevents the full development of the $(\alpha\,\beta\,\gamma)$ phase at the lowest temperatures reached. The annealing time t also plays a role, since for samples S2R and S2A, where this time is smaller, we observe the simultaneous presence of the $(\delta\,\delta\,0)$ and $(\alpha\,\beta\,\gamma)$ phases. From the analysis of the NPD experiments, we can estimate the contribution of each magnetic phase in these samples to be: 22(5)% of $(\delta\,\delta\,0)$ and 78(5)% of $(\alpha\,\beta\,\gamma)$ for S2R, and 74(4)% of $(\delta\,\delta\,0)$ and 26(4)% of $(\alpha\,\beta\,\gamma)$ for S2A.

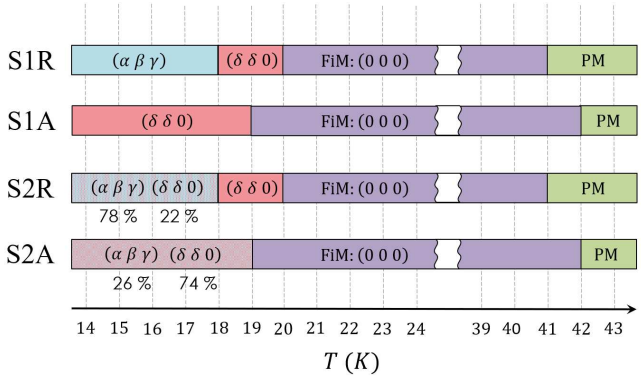

FIG. 11. Magnetic phases observed for each sample together with their phase transition temperatures. Green: paramagnetic order, purple: (0 0 0) - FIM phase, pink: $(\delta\ \delta\ 0)$ - Incommensurate phase, blue: $(\alpha\ \beta\ \gamma)$ - Incommensurate phase. For samples S2R and S2A, the percentages of each incommensurate phase present at the lowest temperature measured is given.

An explanation for the different magnetic ground states observed can be given in terms of the main exchange interactions competing in this system, which we have derived from the analysis of the magnetization data to follow $J_{\mathrm{CrCr}} > J_{\mathrm{CrMn}} > J_{\mathrm{MnMn}}$. Previous works [19, 27, 55] suggested that the interaction between nearest neighbours in B-sites, J_{CrCr}, results from the competition between a strong antiferromagnetic direct exchange between $d-d$ orbitals and an indirect 90° ferromagnetic interaction mediated by O^{2-}-p orbital. Meanwhile, the coupling between A and B-sites, J_{CrMn}, can be explained by a super-exchange Cr^{3+}-O-Mn^{2+} path. For Cr^{3+} ions, with empty e_g orbitals and half-filled t_{2g} orbitals, the 120° J_{CrMn} interaction is antiferromagnetic and weaker relative to the direct overlapping mechanism of the J_{CrCr} interaction. The interaction between A-sites, J_{MnMn}, can be associated with a super-exchange mechanism mediated also by oxygen anions, which gives rise to a weakly antiferromagnetic interaction.

If the J_{CrCr} interaction is dominated by the antiferromagnetic direct exchange term, then magnetic frustration on the B-sites is produced due to their spatial arrangement (pyrochlore sublattice). This frustration can be partially released through the J_{CrMn} interaction, which prevents the Jahn-Teller distortion [19, 22], in agreement with the almost negligible tetragonal and monoclinic distortions observed in our NPD experiments. The interplay between both interactions is expected to produce the transverse conical structure observed in the $(\delta\,\delta\,0)$ phase. As the temperature is decreased, the small J_{MnMn} interaction plays a role in destabilizing the $(\delta\,\delta\,0)$ magnetic ground state and a new distorted transverse conical structure is developed in the $(\alpha\,\beta\,\gamma)$ phase.

The impact of the synthesis conditions on the magnetic structure can be understood by considering the high dependence of J_{CrCr}, J_{CrMn} and J_{MnMn} on the distances between ions, specially for the Mn-O bonds [19, 23]. In the case of the samples S1A and S2A, a small defect ϵ, of Mn^{2+} is present on the A-sites and an excess ϵ of Mn^{2+} appears at the B-sites. In such case, the J_{MnMn} interaction would be weakened, therefore preserving the magnetic ground state developed in the $(\delta\,\delta\,0)$ phase.

By taking into account the calculated value of the exchange interactions, we can also deduce the parameter $u = 4J_{\mathrm{BB}}S_{\mathrm{B}}/3J_{\mathrm{AB}}S_{\mathrm{A}} \approx 2.2$. Previous neutron diffraction studies obtained $u = 1.6$ [29], 2.1 [36], 1.343 [34] and 1.5 [12]. The wide range of values for this parameter can be due to the different synthesis conditions. Nevertheless, all of them satisfy $u > u$" ≈ 1.298, implying an unstable spiral LRO propagating along $\langle 110\rangle$. Tomiyasu *et al.* [12] proposed that such instability is due to a weak magnetic geometrical frustration causing spiral short-range order. In our case, a value of $u = 2.2$, indicating that the $(\delta\,\delta\,0)$ phase is not the ground state, is in agreement with the appearance of the $(\alpha\,\beta\,\gamma)$ phase at lower temperatures.

Although there has been an extensive research on this material [5, 12, 19, 21, 23, 29, 32, 34–38, 44, 53], it has not been until recently that a new low-temperature phase transition has been proposed [32]. There, an incommensurate spiral spin order to a commensurate one (CSSO) transition is suggested, although no hint on the magnetic structure developed in this CSSO is given. As we have shown in this work, this transition is rather from one incommensurate conical to another, where the latest phase has also a incommensurate propagation vector $\vec{k}_{\mathrm{I2}}$. The aforementioned sensitivity to the synthesis conditions can give an explanation on why this $(\alpha\,\beta\,\gamma)$ phase has not been reported before, as in previous studies no special precaution was taken regarding the synthesis of this compound under an oxidizing or reductive atmosphere.

It would be interesting to perform a similar systematic study for the $CoCr_2O_4$ spinel, where some studies have reported the existence of an incommensurate conical structure with propagation vector $(0.63\,0.63\,0)$ below 26 K, and a transition into a commensurate propagation vector $(2/3\ 2/3\ 0)$ plus two satellite peaks with propaga-

tion $(0.035\,0\,0)$ and $(0\,0.035\,0)$ at ~ 14 K [9, 18, 56].

C. Multiferroicity

Previous electric polarization experiments performed in $MnCr_2O_4$ [23, 32] showed that this compound is an improper multiferroic. Those results could be explained by two models, the inverse Dzyaloshinskii-Moriya (DM) [57–59] or the spin current coupling mechanism [60]. In the former model, the spiral magnetic order polarizes an oxygen through the magnetostriction, while in the later one the ferroelectric polarization of the electronic orbitals is induced without the involvement of a spin-lattice interaction. Recently, significant oxygen displacements observed by x-ray powder diffraction suggested that the inverse DM model could be more appropriate to interpret the ferroelectricity observed in ref. [23]. In our results however, the refined structural parameters do not have enough resolution to shed more light into this matter.

Nevertheless, for both models the spontaneous electric polarization is related to the canting of the spins ($\vec{S}_i$ and $\vec{S}_j$) on two neighbouring sites (i and j), and can be mathematically expressed by the same expression:

$$\vec{P} \propto \vec{r}_{ij} \times \left(\vec{S}_i \times \vec{S}_j\right) \tag{3}$$

where $\vec{r}_{ij}$ represents the vector that connects the i and j sites. This polarization can also be expressed in terms of the propagation vector and the net magnetization $\vec{M}_{j,0}$ as in ref. [15, 18]: $\vec{P} \propto \vec{k} \times \vec{M}_{j,0}$. From this expression, it can be observed that a non-zero value of the electric polarization is present for transverse conical (cycloidal) modulations, where the spin rotation axis is not parallel to the propagation vector.

From the viewpoint of the magnetic symmetry, the non-centrosymmetric $Im'a'2(0\,0\,\gamma)0ss$ and $P1(\alpha\,\beta\,\gamma)0$ MSSGs have magnetic point groups ($m'm'2$ and 1, respectively) which allow the presence of such transverse conical structures, which implies the existence of multiferroicity in both $(\delta\,\delta\,0)$ and $(\alpha\,\beta\,\gamma)$ phases. Furthermore, from Table II we can quickly estimate the electric polarization to point along the $\langle 0\,0\,1\rangle$ direction in the $(\delta\,\delta\,0)$ phase, while for the $(\alpha\,\beta\,\gamma)$ phase the spontaneous polarization vector is expected to lie along the $\langle 0\,1\,\bar{3}\rangle$ direction. Such theoretical results are similar to the ones described in [23, 32] for the $(\delta\,\delta\,0)$ phase. However, for the new $(\alpha\,\beta\,\gamma)$ phase our results should be compared with experimental data in order to confirm that the mechanism responsible for the multiferroicity is the same before and after the transition at 18 K.

VI. CONCLUSIONS

The nuclear and magnetic structures of the spinel $MnCr_2O_4$ are reinvestigated as function of the temperature in powder samples synthesized under different conditions by using magnetization, specific heat and NPD experiments.

Through these experiments we confirm the existence of three LRO magnetic phases; a FIM with propagation vector $\vec{k}_{\rm N} = (0\,0\,0)$, an incommensurate spiral phase with $\vec{k}_{\rm I1} = (\delta\,\delta\,0)$, and a new one, never reported, with $\vec{k}_{\rm I2} = (\alpha\,\beta\,\gamma)$. The global symmetry of each magnetic phase was determined using the MSSG formalism.

A possible explanation of the different magnetic ground states observed is given based on the competition among the main exchange interactions present in this system. The transition temperatures of the three LRO magnetic phases depend on the oxidizing or reductive atmosphere in which the samples were synthesized, and a possible explanation of these transitions based on experimental and theoretical results is also discussed. Finally, the presence of transverse conical magnetic structures in both $(\delta\,\delta\,0)$ and $(\alpha\,\beta\,\gamma)$ phases allow the existence of multiferroicity. Using the spin current model, we have derived the direction along which the spontaneous electric polarization should lie for each magnetic phase.

ACKNOWLEDGMENTS

Grant Number PGC2023XM4 funded by MCIN/AEI/10.13039/501100011033 supported this work. Grants OTR02223-SpINS from CSIC/MICIN and DGA/M4 from Diputación General de Aragón (Spain) are also acknowledged. MPS acknowledges a PhD fellowship from the Diputación General de Aragón (Spain).

[1] Z. Lu, J. Zhu, E. A. Payzant, and M. P. Paranthaman, Electrical conductivity of the manganese chromite spinel solid solution, Journal of the American Ceramic Society **88**, 1050 (2005).

[2] H. Li and W. Chen, Stability of $MnCr_2O_4$ spinel and Cr_2O_3 in high temperature carbonaceous environments with varied oxygen partial pressures, Corrosion Science **52**, 2481 (2010).

[3] M. Hamad, Simulated magnetocaloric properties of $MnCr_2O_4$ spinel, Processing and Application of Ceramics **10**, 33 (2016).

[4] S. Chu, Y. Cui, and N. Liu, The path towards sustainable energy, Nature Materials **16**, 16 (2016).

[5] K. Dey, A. Indra, S. Majumdar, and S. Giri, Critical behavior and reversible magnetocaloric effect in multiferroic $MnCr_2O_4$, Journal of Magnetism and Magnetic Materials **435**, 15 (2017).

[6] W. Raza, F. Ali, N. Raza, Y. Luo, K.-H. Kim, J. Yang,

S. Kumar, A. Mehmood, and E. E. Kwon, Recent advancements in super-capacitor technology, Nano Energy **52**, 441 (2018).

[7] K. Manjunatha, V. J. Angadi, R. A. Ribeiro, E. Longo, M. C. Oliveira, M. R. Bomio, S. R. de Lázaro, S. Matteppanavar, S. Rayaprol, P. Babu, and M. Pasha, Structural, electronic, vibrational and magnetic properties of Zn^{2+} substituted $MnCr_2O_4$ nanoparticles, Journal of Magnetism and Magnetic Materials **502**, 166595 (2020).

[8] M. Javed, A. A. Khan, J. Kazmi, M. A. Mohamed, M. S. Ahmed, and Y. Iqbal, Impedance spectroscopic study of charge transport and relaxation mechanism in $MnCr_2O_4$ ceramic chromite, Journal of Alloys and Compounds **854**, 156996 (2021).

[9] S. Funahashi, Y. Morii, and H. R. Child, Two-dimensional neutron diffraction of YFe_2O_4 and $CoCr_2O_4$, Journal of Applied Physics **61**, 4114 (1987).

[10] S. Lee, C. Broholm, W. Ratcliff, G. Gasparovic, Q. Huang, T. H. Kim, and S.-W. Cheong, Emergent excitations in a geometrically frustrated magnet, Nature **418**, 856 (2002).

[11] M. T. Rovers, P. P. Kyriakou, H. A. Dabkowska, G. M. Luke, M. I. Larkin, and A. T. Savici, Muon-spin-relaxation investigation of the spin dynamics of geometrically frustrated chromium spinels, Physical Review B **66**, 10.1103/physrevb.66.174434 (2002).

[12] K. Tomiyasu, J. Fukunaga, and H. Suzuki, Magnetic short-range order and reentrant-spin-glass-like behavior in $CoCr_2O_4$ and $MnCr_2O_4$ by means of neutron scattering and magnetization measurements, Phys. Rev. B **70**, 214434 (2004).

[13] H. Ueda, H. A. Katori, H. Mitamura, T. Goto, and H. Takagi, Magnetic-field induced transition to the 1/2 magnetization plateau state in the geometrically frustrated magnet $CdCr_2O_4$, Physical Review Letters **94**, 10.1103/physrevlett.94.047202 (2005).

[14] J.-H. Chung, M. Matsuda, S.-H. Lee, K. Kakurai, H. Ueda, T. J. Sato, H. Takagi, K.-P. Hong, and S. Park, Statics and dynamics of incommensurate spin order in a geometrically frustrated antiferromagnet $CdCr_2O_4$, Physical Review Letters **95**, 10.1103/physrevlett.95.247204 (2005).

[15] Y. Yamasaki, S. Miyasaka, Y. Kaneko, J.-P. He, T. Arima, , and Y. Tokura, Magnetic reversal of the ferroelectric polarization in a multiferroic spinel oxide, Phys. Rev. Lett. **96**, 207204 (2006).

[16] M. Matsuda, M. Takeda, M. Nakamura, K. Kakurai, A. Oosawa, E. Lelièvre-Berna, J.-H. Chung, H. Ueda, H. Takagi, and S.-H. Lee, Spiral spin structure in the heisenberg pyrochlore magnet $CdCr_2O_4$, Physical Review B **75**, 10.1103/physrevb.75.104415 (2007).

[17] A. N. Yaresko, Electronic band structure and exchange coupling constants in ACr_2X_4 spinels (A=Zn, Cd, Hg; X=O, S, Se), Physical Review B **77**, 10.1103/physrevb.77.115106 (2008).

[18] Y. J. Choi, J. Okamoto, D. J. Huang, K. S. Chao, H. J. Lin, C. T. Chen, M. van Veenendaal, T. A. Kaplan, and S.-W. Cheong, Thermally or magnetically induced polarization reversal in the multiferroic $CoCr_2O_4$, Phys. Rev. Lett. **102**, 067601 (2009).

[19] E. Winkler, S. Blanco Canosa, F. Rivadulla, M. A. López-Quintela, J. Rivas, A. Caneiro, M. T. Causa, and M. Tovar, Magnetocrystalline interactions in $MnCr_2O_4$ spinel, Phys. Rev. B **80**, 104418 (2009).

[20] K. Tomiyasu, K. Horigane, T. Yokobori, Y. Kousaka, M. Takahashi, H. Hiraka, J. Akimitsu, and K. Yamada, Unquenched geometric frustration effect on spiral spin correlation in magnetically ordered phase, Journal of the Physical Society of Japan **78**, 084704 (2009).

[21] N. Mufti, A. A. Nugroho, G. R. Blake, and T. T. M. Palstra, Magnetodielectric coupling in frustrated spin systems: the spinels MCr_2O_4 (M = Mn, Co and Ni), Journal of Physics: Condensed Matter **22**, 075902 (2010).

[22] V. Kocsis, S. Bordács, D. Varjas, K. Penc, A. Abouelsayed, C. A. Kuntscher, K. Ohgushi, Y. Tokura, and I. Kézsmárki, Magnetoelasticity in ACr_2O_4 spinel oxides (A=Mn, Fe, Co, Ni, and Cu), Phys. Rev. B **87**, 064416 (2013).

[23] K. Dey, S. Majumdar, and S. Giri, Ferroelectricity in spiral short-range-ordered magnetic state of spinel $MnCr_2O_4$: Significance of topological frustration and magnetoelastic coupling, Physical Review B **90**, 10.1103/physrevb.90.184424 (2014).

[24] Y. Li, S. Feng, Q. Lv, X. Kan, and X. Liu, An investigation of reentrant spin-glass behavior, magnetocaloric effect and critical behavior of $MnCr_2O_4$, Journal of Alloys and Compounds **877**, 160224 (2021).

[25] F. F. Fava, I. Baraille, A. Lichanot, C. Larrieu, and R. Dovesi, On the structural, electronic and magnetic properties of $MnCr_2O_4$ spinel, Journal of Physics: Condensed Matter **9**, 10715 (1997).

[26] T. Suzuki, K. Adachi, and T. Katsufuji, Correlation between magnetic, dielectric properties and crystal structure in MnT_2O_4 (T=V, Cr, Mn), Journal of Magnetism and Magnetic Materials **310**, 780 (2007).

[27] C. Ederer and M. Komelj, Magnetic coupling in $CoCr_2O_4$ and $MnCr_2O_4$: An LSDA + U study, Phys. Rev. B **76**, 064409 (2007).

[28] S. Blanco-Canosa, F. Rivadulla, V. Pardo, D. Baldomir, J.-S. Zhou, M. García-Hernández, M. A. López-Quintela, J. Rivas, and J. B. Goodenough, Enhanced pressure dependence of magnetic exchange in $A^{2+}[V_2]O_4$ spinels approaching the itinerant electron limit, Phys. Rev. Lett. **99**, 187201 (2007).

[29] J. M. Hastings and L. M. Corliss, Magnetic structure of manganese chromite, Phys. Rev. **126**, 556 (1962).

[30] H. Gupta, M. Sinha, Balram, and B. Tripathi, A study of the interatomic interaction in oxide spinel $MnCr_2O_4$, Physica B: Condensed Matter **192**, 343 (1993).

[31] S. Bordács, D. Varjas, I. Kézsmárki, G. Mihály, L. Baldassarre, A. Abouelsayed, C. A. Kuntscher, K. Ohgushi, and Y. Tokura, Magnetic-order-induced crystal symmetry lowering in ACr_2O_4 ferrimagnetic spinels, Physical Review Letters **103**, 10.1103/physrevlett.103.077205 (2009).

[32] G. T. Lin, Y. Q. Wang, X. Luo, J. Ma, H. L. Zhuang, D. Qian, L. H. Yin, F. C. Chen, J. Yan, R. R. Zhang, S. L. Zhang, W. Tong, W. H. Song, P. Tong, X. B. Zhu, and Y. P. Sun, Magnetoelectric and raman spectroscopic studies of monocrystalline $MnCr_2O_4$, Physical Review B **97**, 10.1103/physrevb.97.064405 (2018).

[33] D. H. Lyons, T. A. Kaplan, K. Dwight, and N. Menyuk, Classical theory of the ground spin-state in cubic spinels, Physical Review **126**, 540 (1962).

[34] R. Plumier, Reinvestigation of magnetic structures of $CoCr_2O_4$ and $MnCr_2O_4$ obtained by neutron diffraction, Journal of Applied Physics **39**, 635 (1968), https://doi.org/10.1063/1.2163559.

[35] Y. Zhou, Z. Yang, L. Li, Y. Xie, S. Lin, Y. Sun, and Y. Zhang, Magnetic field and external pressure effects on the spiral order of polycrystalline $MnCr_2O_4$, Journal of Magnetism and Magnetic Materials **324**, 3799 (2012).

[36] K. Dwight, N. Menyuk, J. Feinleib, and A. Wold, Reduced manganese moment in manganese chromite, Journal of Applied Physics **37**, 962 (1966), https://doi.org/10.1063/1.1708539.

[37] D. Tobia, J. Milano, M. T. Causa, and E. L. Winkler, Temperature evolution of the effective magnetic anisotropy in the $MnCr_2O_4$ spinel, Journal of Physics: Condensed Matter **27**, 016003 (2015).

[38] N. Mufti, G. Blake, and T. Palstra, Magnetodielectric coupling in $MnCr_2O_4$ spinel, Journal of Magnetism and Magnetic Materials **321**, 1767 (2009).

[39] A. Janner and T. Janssen, Symmetry of incommensurate crystal phases. I. Commensurate basic structures, Acta Crystallographica Section A **36**, 399 (1980).

[40] J. M. Perez-Mato, J. L. Ribeiro, V. Petricek, and M. I. Aroyo, Magnetic superspace groups and symmetry constraints in incommensurate magnetic phases, Journal of Physics: Condensed Matter **24**, 163201 (2012).

[41] J. Rodríguez-Carvajal and J. Villain, Magnetic structures, Comptes Rendus Physique **20**, 770 (2019).

[42] L. Néel, Antiferromagnetism and ferrimagnetism, Proceedings of the Physical Society. Section A **65**, 869 (1952).

[43] F. Lotgering, On the ferrimagnetism of some sulphides and oxides, Philips Research Reports **11**, 190 (1956).

[44] G. Lin, W. Tong, X. Luo, F. Chen, L. Yin, Y. Wang, L. Hu, Y. Zou, L. Yu, W. Song, and Y. Sun, Magnetocrystalline interactions in spinel $MnCr_2O_4$ single crystal probed by electron spin resonance, Journal of Alloys and Compounds **711**, 250 (2017).

[45] J. Rodríguez-Carvajal, Recent advances in magnetic structure determination by neutron powder diffraction, Physica B: Condensed Matter **192**, 55 (1993).

[46] H. T. Stokes, D. M. Hatch, and B. J. Campbell, ISODISTORT, ISOTROPY software suite, iso.byu.edu (2017).

[47] B. J. Campbell, H. T. Stokes, D. E. Tanner, and D. M. Hatch, ISODISPLACE: a web-based tool for exploring structural distortions, Journal of Applied Crystallography **39**, 607 (2006).

[48] M. I. Aroyo, J. M. Perez-Mato, D. Orobengoa, E. Tasci, G. de la Flor, and A. Kirov, Crystallography online: Bilbao Crystallographic Server, Bulgarian Chemical Communications **43**, 183 (2011).

[49] M. I. Aroyo, J. M. Perez-Mato, C. Capillas, E. Kroumova, S. Ivantchev, G. Madariaga, A. Kirov, and H. Wondratschek, Bilbao Crystallographic Server: I. Databases and crystallographic computing programs, Zeitschrift fur Kristallographie - Crystalline Materials **221**, 10.1524/zkri.2006.221.1.15 (2006).

[50] M. I. Aroyo, A. Kirov, C. Capillas, J. M. Perez-Mato, and H. Wondratschek, Bilbao Crystallographic Server. II. Representations of crystallographic point groups and space groups, Acta Crystallographica Section A Foundations of Crystallography **62**, 115 (2006).

[51] J. Perez-Mato, S. Gallego, E. Tasci, L. Elcoro, G. de la Flor, and M. Aroyo, Symmetry-based computational tools for magnetic crystallography, Annual Review of Materials Research **45**, 217 (2015).

[52] R. E. Newnham and Y. M. de Haan, Refinement of the α Al_2O_3 , Ti_2O_3 , V_2O_3 and Cr_2O_3 structures, Zeitschrift fur Kristallographie **117**, 235 (1962).

[53] N. Menyuk, K. Dwight, and A. Wold, Ferrimagnetic spiral configurations in cobalt chromite, Journal de Physique **25**, 528 (1964).

[54] E. Whipple and A. Wold, Preparation of stoicheiometric chromites, Journal of Inorganic and Nuclear Chemistry **24**, 23 (1962).

[55] D. G. Wickham and J. B. Goodenough, Suggestion concerning magnetic interactions in spinels, Phys. Rev. **115**, 1156 (1959).

[56] L. J. Chang, D. J. Huang, W.-H. Li, S.-W. Cheong, W. Ratcliff, and J. W. Lynn, Crossover from incommensurate to commensurate magnetic orderings in $CoCr_2O_4$, Journal of Physics: Condensed Matter **21**, 456008 (2009).

[57] I. Dzyaloshinsky, A thermodynamic theory of "weak" ferromagnetism of antiferromagnetics, Journal of Physics and Chemistry of Solids **4**, 241 (1958).

[58] T. Moriya, Anisotropic superexchange interaction and weak ferromagnetism, Phys. Rev. **120**, 91 (1960).

[59] I. A. Sergienko and E. Dagotto, Role of the Dzyaloshinskii-Moriya interaction in multiferroic perovskites, Phys. Rev. B **73**, 094434 (2006).

[60] H. Katsura, N. Nagaosa, and A. V. Balatsky, Spin current and magnetoelectric effect in noncollinear magnets, Phys. Rev. Lett. **95**, 057205 (2005).